Catalyst dissolution in PEM water electrolysis: Influence of time, current density and Iridium ion transport in single-pass and recirculation water flow modes

An Phuc Dam [a] , Tobias Franz [b] , Georgios Papakonstantinou [a], Kai Sundmacher [a,b,*]

[a] *Max Planck Institute for Dynamics of Complex Technical Systems, Process Systems Engineering, Sandtorstraße 1, Magdeburg D-39106, Germany*
[b] *Otto, von-Guericke University Magdeburg, Process Systems Engineering, Universitätsplatz 2, Magdeburg D-39106, Germany*

A B S T R A C T

The current study targets three major aspects central to the phenomenon of Iridium (Ir) catalyst dissolution in polymer electrolyte membrane water electrolyzers; the stabilization over time, the influence of current density and the mechanisms of transport and deposition of dissolved Ir species. Quasi-online measurements of Ir dissolution at the anode side of single-cells using single-pass water flow reveal that oxygen molecules produced per Ir dissolved increases by up to two orders of magnitude with current density and then level off. Experiments under water recirculation show that Ir ions are back-transported into the catalyst coated membrane. Model-aided analysis suggests that Ir species re-deposited into the catalyst layer are stabilized at elevated concentrations of dissolved Ir ions. Application of single-pass flow is recommended for stability testing. An observed stabilization of over two orders of magnitude with time provides promising insight into the applicability of low Ir loadings under steady-state conditions.

1. Introduction

Polymer electrolyte membrane water electrolysis (PEMWE) is a key technology for the storage of intermittent renewable energy through the production of green hydrogen. Due to strong acidity and high anodic potentials, only iridium-based materials have so far been found to possess the necessary electrocatalytic activity and stability for the oxygen evolution reaction (OER). However, due to the scarcity of the noble metal iridium (Ir), the catalyst loading has to be significantly reduced [1–4]. Low loadings pose serious challenges to Ir-based catalyst materials due to dissolution and catalyst degradation [5]. Fundamental insights into the phenomena of Ir dissolution have been obtained by investigations in aqueous model systems, i.e. half-cells with liquid electrolyte [6–11]. It is suggested that the dissolution under OER potentials is closely coupled to the OER, proceeding through a shared surface intermediate state [7,12] that is thermodynamically unstable [13]. Isotope labelling experiments indicate that lattice-oxygen participation in the OER disrupts the lattice structure [6]. This disruption leads to the simultaneous release of anionic and cationic Ir species [14]. Although identifying the exact speciation of the dissolution species

remains challenging, IrO_4^{2-} or $Ir(OH)_6^{2-}$ have been proposed as possible anionic Ir species [14–17], while cationic products are generally presumed to exist as Ir^{3+} [7,18,19]. However, there is a large discrepancy in the stability-number, i.e. the amount of oxygen produced per Ir atom dissolved, between half-cell and zero-gap membrane electrode assemblies (MEAs). In half-cells, hydrous quasi-crystalline IrOx catalysts exhibit stability-numbers of around 10^5 [6,20], whereas four orders of magnitudes higher values are reported in MEA-setups [14,21,22]. Long-term electrochemical tests, e.g. up to 4500 h [23,24], are important for the assessment of overlapping degradation modes [5,25] in the full system. However, even these time frames cannot reliably predict a lifetime of e.g. 10 years (87600 h), and these tests do not specifically target Ir dissolution. Therefore, it is essential to perform dissolution studies in the MEA-setup and develop methods that allow for the quantification of Ir dissolution in this environment. In this way, a systematic assessment of the electrocatalytic stability can be performed, which will aid in the development of the catalytic material and the optimization of the system design [26–28] in order to realize tangible improvements of industrial electrolyzers [29].

The quantification of Ir dissolution in the zero-gap MEA environment

is challenging. In the literature, catalyst-coated membranes (CCMs) from the MEA-setup are commonly analyzed post-test using microscopic techniques, which provide valuable insights [23,25,30]. However, quantitative analysis at the different locations is challenging as Ir can be either in ionic form or deposited in different regions of the CCM, which is neither homogeneous nor void-free. Recently, the amount of Ir transported to and deposited in the cathode catalyst layer (CCL) at the end of test has been quantified by dissolution in aqua regia [31]. However, the species deposited in the membrane domain form an Ir band near the anode catalyst layer (ACL) [23,25,32], limiting the effectiveness of this method to shorter operating times as an increasing fraction of Ir ions moving in the cathode direction is blocked. Therefore, understanding the transport and deposition mechanisms of Ir ions is crucial for the interpretation of dissolution data obtained by different quantification methods, such as sampling from the water lines [21,33] or post-test analysis of the CCMs [34–36]. Furthermore, the transport of dissolved catalyst species is of direct technical importance, since the presence of dissolved catalyst species may reduce the loss of catalyst material by redeposition in the anode catalyst layer (ACL) or by reducing the driving force for dissolution due to a concentration-induced shift in the Nernst potential of the corrosion process [6,37,38]. The transport mechanisms also determine whether and how Ir can be recycled from the CCMs [39,40] at the end of life of the PEMWE stacks. It has been shown that the transport of Ir dissolution products is strongly influenced by the charge of the Ir ions, which determines both the direction of the migration driving force and the probability of the Ir ions either being absorbed in the ionomer/membrane or dissolved in the water phase [14].

In this study, three influences central to the phenomenon of Ir dissolution are investigated in the MEA setup: the impact of operating time, the effect of current density, and the transport and deposition behavior of Ir dissolution products. The current density dependence can provide mechanistic insights into the dissolution of Ir during OER [12]. Investigations in half-cells [20,41] and MEA-setups with recirculated water flow [21] have suggested that the operating time plays a key role in the differences in dissolution between the two environments [6]. The influences of time and current density are herein studied in single-pass water flow mode, which allows quasi-online measurement of Ir dissolution in the anode water line and minimizes sink terms for water-dissolved Ir species. The transport and deposition behavior of water-dissolved Ir species is examined by switching between water recirculation and single-pass flow modes and measuring Ir concentration over time. It is observed that dissolved Ir is transported back into the CCM during water recirculation mode, and model-aided analysis provides further insight into the nature of this process. The clear evidence of a significant sink term with recirculated water flow for both Ir cations and anions underscores that single-pass water flow is preferable for assessing electrocatalytic stability. Based on the single-pass approach, an ACL lifetime analysis is performed considering different catalyst loadings and current densities.

2. Methodology

2.1. Test station and MEA specifications

Electrochemical and catalyst dissolution experiments are mainly performed in 'test station A' with a PEMWE single-cell (active area 24.85 cm^2). A commercial CCM from Ion Power GmbH with Ir loading 0.5 mg/cm^2 (IrOx, Alfar Aesar, product number 43396), Nafion 117 membrane and Pt/C cathode catalyst layer with Pt loading 0.2 mg/cm^2 is used. The ionomer content is 21 and 25 wt% in the anode and cathode catalyst layers, respectively. A Pt-coated porous transport layer (PTL) from NV Bekaert SA with 79 % porosity and an uncompressed thickness of 1 mm was applied together with titanium (Ti, grade 2) flow fields. A hydrophobized carbon gas diffusion layer from Freudenberg (E20H) was used on the cathode side. An AMETEK Solartron Analytical EnergyLab

XM ECS potentiostat with a 20 A booster was used at current densities below 0.8 A/cm^2, while at higher current densities an electronic load (Höcherl & Hackl, 9186D-0614, 0–150 A) set to constant current mode was connected in series with a constant voltage source (Statron 2257.8). Unless otherwise noted, experimental data were obtained in test station A. Additional tests were conducted in 'test station B' using a Horiba-FuelCon 70460 test station, with modified anode water lines to allow for single-pass flow mode. CCMs (QuinTech) with active area of 8.4 cm^2 were employed, comprising a Nafion N212 membrane and the same catalyst material (Ir loading 1 mg/cm^2 and Pt loading 0.3 mg/cm^2).

2.2. Electrochemical testing and operating conditions

A water flow rate of 0.8 mL/(min•cm^2) was applied to the anode side in test station A (Test station B, 0.6 mL/(min•cm^2)), unless otherwise stated. The temperature was measured at the anode cell inlet and outlet as well as inside the current collector at a distance of ca. 3.5 mm from the ACL (ca. 2 mm, test station B). The cell temperature in test station A was determined by the temperature-controlled inlet water flow and the applied current density (Figure S1, S2, S3, and S4). The single cell in test station B was thermostated at 80°C via two heating cartridges, each with its own individual control circuit. Polarization was galvanostatic unless otherwise stated. For testing at low current densities, the cathode side was continuously flushed with hydrogen at 50 mL/min in order to maintain a well-defined potential of the cathode electrode. The cathode side was always flushed with nitrogen during open circuit periods longer than five minutes to prevent chemical reduction of the Ir oxide catalyst by permeating H$_2$.

2.3. Ir dissolution testing and water flow modes

In order to minimize the possibility of Ir ion deposition on metal surfaces via galvanic displacement [33], either plastic or PTFE-based materials were used in both test stations, with the exception of the cell itself. Both PEMWE test stations allow two different water-feed modes to the anode side (Fig. 1), (a) in recirculation, and (b) in single-pass, from a temperature-controlled water tank containing purified water (0.055 μS/cm). Water was collected either in plastic containers or in small plastic tubes (sample volume ca. 6 mL) to measure the Ir concentration. Water transported to the cathode side by electroosmotic drag was collected from the condenser at the cathode outlet (Fig. 1) for quantification of Ir. During testing in recirculation flow mode in test station A (Section 3.3), the water volume was either kept constant by refilling the bubbler with fresh water or allowed to decrease without refilling. No heating was applied during the water recirculation test,
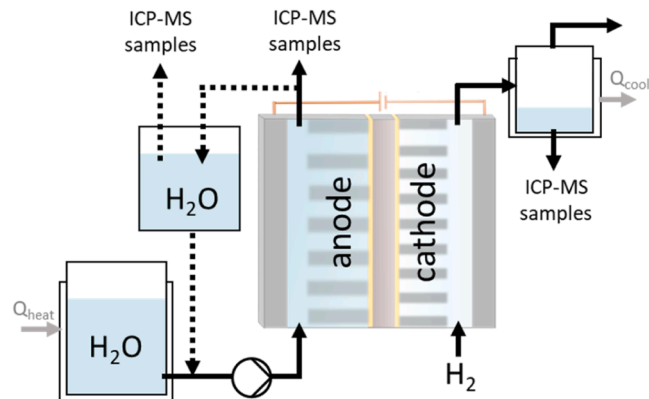
Fig. 1. Schematic illustrating the single-pass water flow mode (solid line path) of the anode water line for both test station A and test station B. In this flow mode, the anode side is supplied with temperature-controlled purified water from an external source. Also shown is the recirculation flow mode (dashed line path) used for specific experiments discussed in Section 3.3.

resulting in a steady-state cell temperature of ca. 34°C.

Iridium was quantified by inductively coupled plasma mass spectrometry (ICP-MS, PlasmaQuant MS Elite, Analytik Jena GmbH & Co KG). A 5-point calibration was performed prior to each measurement series. A standard solution was measured after ca. 4–5 samples to detect and correct possible signal drifts. For samples with very low Ir concentrations, water was evaporated at 80 °C in order to reduce the volume from 40 to 5 mL to ensure that the quantification limits of the ICP-MS are met. Ion chromatography (Thermo Scientific Dionex Aquion IC system) was used to quantify cationic and anionic impurities that accumulate in the bubbler during operation with water recirculation. To test the ionic charge of the dissolution products, absorption tests were conducted by immersing a 5.5 cm^2 piece of Nafion 117 cation exchange membrane (CEM) in 30 mL of solution containing Ir dissolution products. The absorbed fraction is defined as the amount of Ir absorbed, measured by sampling after ca. 9 days, divided by the amount of Ir initially present in the solution [14].

2.4. Mathematical modelling of transport and deposition of Ir anions

A dynamic model is developed to describe the dissolution, transport, and deposition of Ir in the recirculated anode water line (more details on the model development in SI Section 5). Only anionic Ir species are considered, as the cationic fraction becomes negligible with increased operating time (Section 3.3.1 and Figure S21). The schematic of the model (Fig. 2) shows the water domain (blue lines) in which the amount of dissolved anionic Ir species is balanced. This domain is considered as ideally-mixed. Three different sinks are considered in the model: 1) deposition of Ir anions on the Ti flow field, $\sigma_{dep,FF,m}$, 2) on the PTL, $\sigma_{dep,PTL,m}$, and 3) back-transport of Ir species into the CCM, $\sigma_{bt,m-}$.

The transport back into the CCM, $\sigma_{bt,m-}$, includes both the deposition of Ir ions within the ACL region and/or the possibility that the Ir species remain in ionic form and are transported further in the cathode direction (eqn. S13). Point 3 is discussed in more detail in Section 3.3.3. The deposition rate constants on the Ti flow field and the PTL were estimated by performing separate Ir deposition tests (SI Section 7). Two parameters are identified by fitting the model to the measured dynamic Ir concentration profile: The rate constant $k_{bt,m-}$ describing the generic transport of Ir anions back into the CCM (eqn. S17), and the stability-number, $S_{N,w}$.

3. Results and discussion

3.1. Influence of time on catalyst dissolution

To study the influence of time and current density on catalyst dissolution, the single-pass flow mode was used, which allows for quasi-
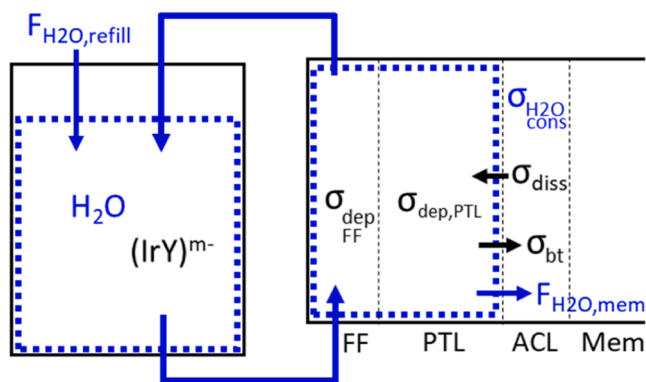

Fig. 2. Schematic representation of the dynamic model describing the dissolution, transport and deposition of Ir anions in the water phase. The model equations are given in SI Section 5.

online measurements and minimizes sink effects, as discussed in Section 3.3. Figure S4 shows the Ir dissolution flux during the first 220 min of operation directly after cell assembly. A significant increase in the Ir dissolution rate is observed after the start of cyclic voltammetry (CV), linked to the reduction and re-oxidation processes of the catalyst surface under cycling below OER potentials [20,42]. The dissolution rate, normalized by the CV charge, is ca. three times lower than that seen in half-cells under similar cycling conditions (0.4–1.4 V vs. reversible hydrogen electrode, RHE) [20]. This lower dissolution flux in the MEA-setup could be due to a higher likelihood of dissolved Ir ions, which are predominantly cationic when dissolved in the low potential region, to be absorbed into the ionomer phase in the MEA environment [6,14]. However, the relatively small difference between the two environments underscores that the Ir oxide does not exhibit much higher stability in the MEA environment as a general characteristic, but the orders of magnitude difference in stability between the two setups [6,21] is apparent to the OER potential region.

In procedure 1, the initial potential increase above the onset of the OER leads to a significant rise in the dissolution rate (Figure S4) due to the coupling between Ir dissolution and OER [6,7], even at a low current density of 5 mA/cm^2. The Ir dissolution flux decreases significantly with time. Meanwhile, sharp dissolution peaks occur in the first staircase (Fig. 3a) immediately after each increase in current density. However, these sharp dissolution peaks are already absent during the second staircase (procedure 3). The green circles in Fig. 3 signify that the concentration range has been exceeded in one (or rarely two) of the five sub-measurements, indicating the presence of nanoparticles in the solution due to particle detachment. For these data points, the displayed value is the average of the remaining sub-measurements. Particle detachment tends to occur simultaneously with the current density steps. However, it is not observed after the first two staircases, consistent with reports suggesting that mechanical detachment of particles contributes only a minor fraction of the total loss of Ir catalyst material [14,43]. As the system is still strongly stabilizing, there is no clear trend between Ir dissolution rate and current density during procedure 2 (Figure S5a). A clearer correlation between Ir dissolution and current density is observed with increasing operating time, as shown by the measurements during procedure 3 (Figure S5b) and procedure 5 (Fig. 5a), despite some scatter in the dissolution data.

Fig. 4 shows that even with the use of single-pass water flow to prevent sinks for Ir ions, the stability-number measured in the anode water line increases by more than two orders of magnitude with time in both test stations, consistent with previous observations under recirculating water flow [21]. For t > 1 h, the time-dependent stabilization process can be described by Eq. 1, as shown in Fig. 4 and Figure S6 in terms of stability-number ($S_{N,w}$) and dissolution rate ($\dot{n}_{Ir}$), respectively.

$$\dot{n}_{Ir} = \frac{A}{1 + B\,t} \tag{1}$$

This mathematical formulation reproduces the similarity of the slopes (Fig. 4, solid lines) via the common $1/t$ dependence, which results in $d(\log S_N)/d(\log t) = 1$. In SI Section 3 it is shown that this reciprocal dependence can be derived from a mechanistic model in which the surface is kinetically stabilized by a reaction that exhibits a quadratic order with respect to the density of unstable sites (eqn. S2).

The quadratic reaction order can result from a bi-nuclear stabilization reaction step. Furthermore, adsorption (oxidation) processes can exhibit a quadratic reaction order if multiple sites are deactivated per occurring adsorption event, with the number of deactivated sites per adsorption event being proportional to the site density [44]. Conversely, it is found that a simple model of the stabilization process, in which the number of unstable sites S is directly reduced by the dissolution reaction (Eq. S5), fails to replicate the observed reciprocal dependence (SI Section 3).
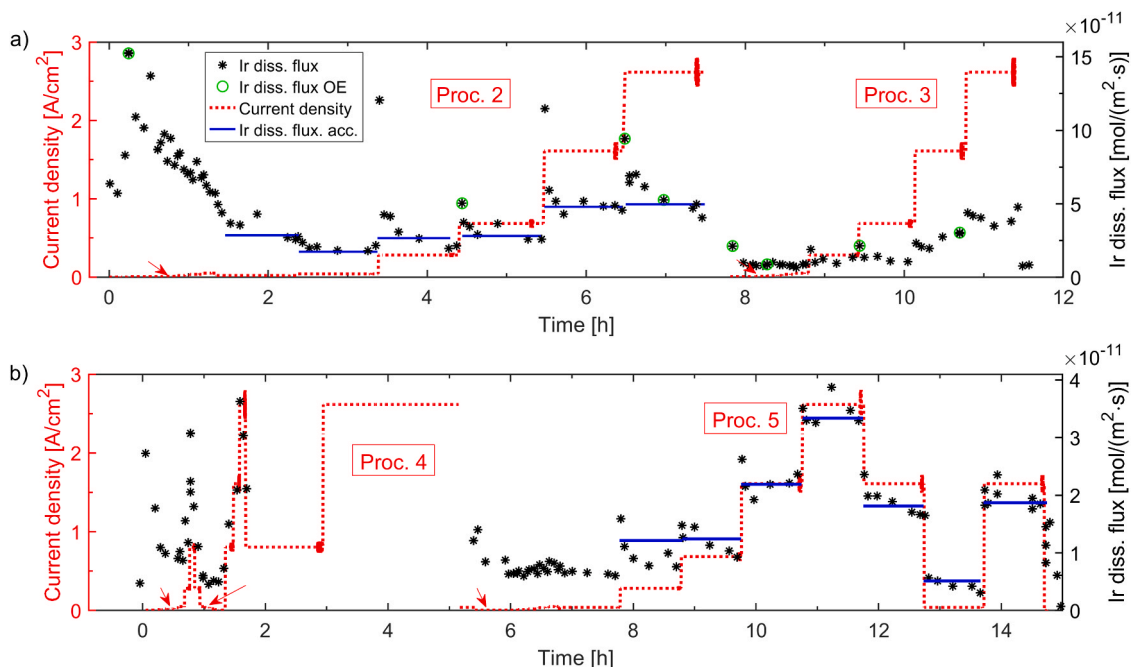
Fig. 3. Current density (red dashed lines) and resulting Ir dissolution fluxes (black stars) in the anode water effluent against the time of different operating procedures. Black stars depict the small volume samples (ca. 6 mL) and blue lines represent the cumulative anode effluent water. Green circles mark ICP-MS data where one sub-measurement (or rarely two) exceeded the detector range. Red arrows indicate staircase polarizations in the low current density region (current density in log-scale in Fig. S2 and Fig. S3). The Ir dissolution flux is calculated by dividing the measured Ir dissolution flow by the active area of the cell.
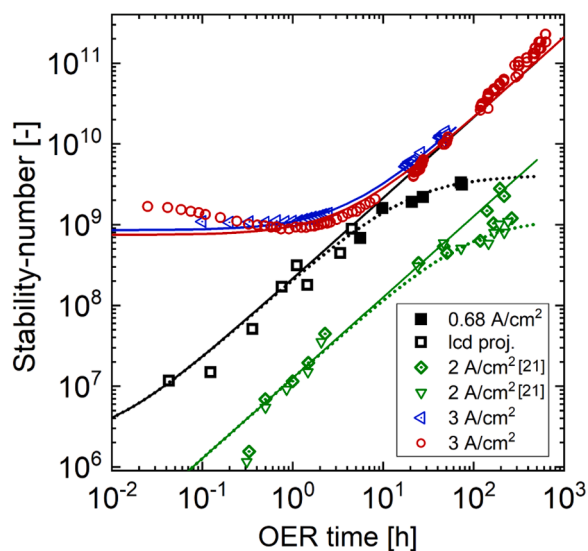
Fig. 4. Stability-number versus OER time. Open squared symbols represent measurements at low current densities and are projected to the current density of 0.68 A/cm^2 by utilizing the relationship between the stability-number and current density, depicted in Fig. 6. Using the same QSS relation, the stability-numbers recorded at 2 A/cm^2 (green) and 3 A/cm^2 (red and blue symbols) are also projected to 0.68 A/cm^2 by dividing by a factor of 1.3. The data measured at 3 A/cm^2 were obtained in test station B. The data at 2 A/cm^2 were obtained from the water recirculation loop and are taken from [21]. Low potential (E < 1.4 V) and OCP phases are not included in the time-axis (relevant only for the black symbols). The solid lines represent the fit of Eq. 1. The dotted lines incorporate an additional steady-state contribution term $\dot{n}_{Ir,SS}$ as described in eqn. S1.

3.2. Quasi-steady-state dependence of Ir dissolution on current density/potential

As pointed out in Section 3.1, a quasi-steady-state (QSS) relationship between Ir dissolution rate and current density becomes more apparent with increasing operating time (Fig. 5a), as the influence of time becomes small compared to the effect of changing the current density. The selected sequence of current density steps demonstrates that the QSS relationship is essentially maintained regardless of the polarization direction when the MEA is in a stabilized state.

These observations are consistent with the understanding of a common surface state of OER and catalyst dissolution during the OER catalytic cycle, resulting in a QSS relationship of dissolution rate versus current density [6,7,12,17], and extend the mechanistic understanding from the half-cell to the MEA environment. In the low current range, the dissolution rate exhibits a weak sensitivity to current density, although the latter is changed by ca. one order of magnitude (Figure S7). At higher currents, however, the dissolution flux seems to scale linearly with current density and, consequently, exponentially with potential (Fig. 5b).

The slight upward curvature of the Ir dissolution flux at high current densities (Fig. 5a) can be rationalized by the increasing cell temperature with current (Figure S3b). Correcting for the effect of temperature using the Arrhenius equation and an apparent activation energy of 43 kJ/mol (Figure S8) eliminates the slight upward curvature, as evidenced by the lowest dissolution flux values at each current density level (Figure S9), which are less affected by transient behavior during changes in current density. The linearity between current density and catalyst dissolution has been attributed to the direct competition of the chemical rate-determining step of the OER with a chemical dissolution step [12], and results in a plateau of the stability-number at high currents (Fig. 6a).

Similar qualitative characteristics have also been observed in half-cell setups, but with orders of magnitude difference in the stability-number [6,7]. The sensitivity of the stability-number to the current density appears to be much greater in the MEA-setup than in half-cells [6]. It leads to a remarkable increase of two orders of magnitude
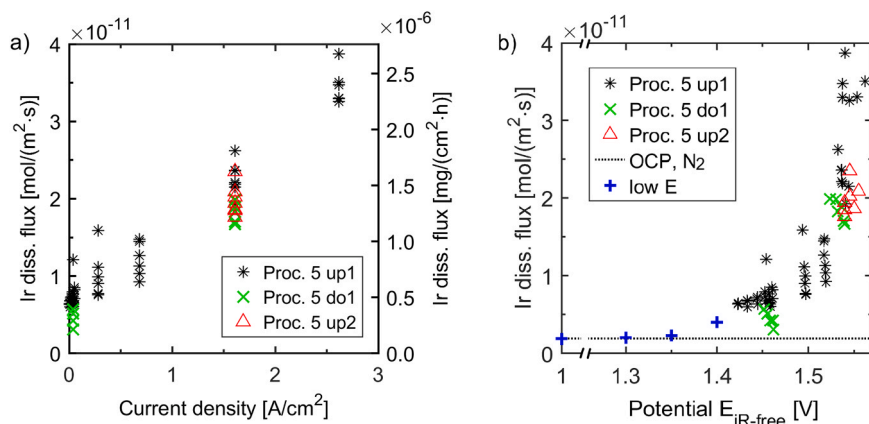
Fig. 5. Ir dissolution flux towards the anode flow field channels, a) against current density, and b) against iR-free potential. All measurements were conducted at an elevated cell temperature with a hydrogen atmosphere on the cathode side, except for the data point represented by the dotted line in (b), which was measured under open-circuit conditions with nitrogen on the cathode side. The blue crosses and the dotted line are taken from Fig. S14 and correspond to the last Ir dissolution flux of each potential step.
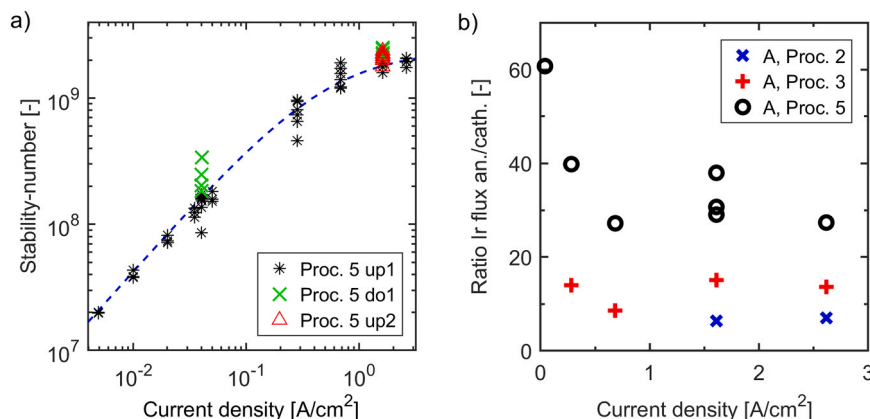
Fig. 6. a) Stability-number values measured during procedure 5. The blue dashed line displays the empirical correlation given by eqn. S39. b) Ratio of Ir dissolution flux towards the anode flow field over that towards the cathode flow field vs. current density.

(Fig. 6a). The high sensitivity of the stability-number compared to the half-cell setup is related to the much lower Tafel slope exhibited by the OER in the MEA setup (ca. 35 mV/dec, Figure S 10), combined with the low sensitivity of the dissolution rate at low current densities exhibited in both environments [12]. The dependence of the stability-number on current density, which extends over orders of magnitudes, was also confirmed in test station B (Figure S13).

A small but significant Ir dissolution flux is observed at low cell potentials (Fig. 4b), even when the potential remains constant and below the apparent OER onset. Figure S14 shows that this Ir dissolution flux does not decline rapidly, but persists even after 3 hours. It is similar whether the cathode side is in a nitrogen atmosphere with the cell open-circuited, or the cathode side is in a hydrogen atmosphere with an applied voltage of 1.3 or 1.35 V (Fig. 5b), but diminishes as the cell cools down (Figure S14). Therefore, the primary driver of this Ir dissolution flux appears to be the elevated cell temperature.

As catalyst stabilization progresses, the Ir dissolution flow to the cathode outlet scales approximately linearly with current density (Fig. 6b and Figure S15b), mirroring observations on the anode side. Measurements also on the cathode side reveal an upward bending of the Ir dissolution flux at high current densities (Figure S16) due to the rise in cell temperature. The electroosmotic drag factor, i.e. the number of water molecules per number of protons transported to the cathode side, is roughly the same (ca. 2) for different current densities (Figure S17). An increase in the anode/cathode Ir dissolution flux ratio towards very

low current densities can be explained by a reduced transport velocity to the cathode side due to decreasing electroosmotic drag and migration. The Ir dissolution flux arriving at the cathode flow field is much smaller than that arriving at the anode flow field by at least one order of magnitude because a large fraction of the Ir ions transported in the cathode direction is deposited within the CCM [23,31].

3.3. Analysis of transport and sinks of water-dissolved Ir ions

3.3.1. Transport of Ir cations and anions in single-pass and recirculation flow modes

The participation of lattice oxygen during OER leads to destabilization and rupture of the lattice structure [6], resulting in the simultaneous generation of cationic and anionic Ir dissolution products [14]. This view is supported by a two-step absorption experiment with the single-pass anode water effluent, which shows selective absorption of the cationic species during the first absorption step (ca. 0.25–0.3) and a negligible absorption fraction in the second step with a pristine membrane (Figure S18). The cationic fraction of Ir in the anode water line under single-pass flow is roughly constant with time once the system is in a stabilized state (Figure S19).

Both Ir cations and anions are present in the cathode water line, as evidenced by the absorption fraction of approximately 0.4 for dissolved Iridium from this water line in the CEM (Figure S20). However, the fluxes are much smaller than those into the anode water line (Fig. 6b).

Only a minor fraction of the Ir anions is transported to the cathode side for several reasons: a) The species have a low affinity for absorption in the ionomer and membrane phases. Therefore, in single-pass flow mode, the water-dissolved species are quickly carried out of the system due to the strong bubbling conditions [14], as illustrated in Fig. 7. b) The migration force pushes them in the anode direction [45], and c) large Ir anions, e.g. IrO_4^{2-} [7,17], require wider channels for transport, which become increasingly rare near the ACL with increasing growth of the 'Ir band' [23,25,36]. The small amount of anionic Ir that is transported to the cathode side, if not deposited in the CCL, can easily leave the cathode catalyst layer due to its low affinity to be absorbed in the membrane or ionomer phase (low partition coefficient $K_p = c_{Ir,mem}/c_{Ir,sol}$ [46,47]).

The transport of cationic species out of the CCM on both the anode and cathode sides, despite their high partition coefficient, can be rationalized by a fast interfacial absorption/desorption equilibrium, which is often considered to occur instantaneously [48–50]. Even a very low equilibrium concentration of Ir cations on the water side of the interfacial boundary can trigger a significant release of species from the ionomer phase in single-pass flow mode, provided that these species are rapidly transported away. Vigorous bubbling on both the anode and cathode sides greatly enhances the transport of the water-dissolved ions. It is noted that there may also be differences in partition coefficients between the cationic Ir species, which would affect their likelihood of leaving the CCM. It has been observed that a small fraction of Ir dissolved in 0.1 M $HClO_4$ under OER conditions was absorbed by a cation exchange resin but not by a CEM, regardless of the amount of ion exchange material [14].

Under water recirculation conditions, the cationic fraction of dissolved Ir in the anode water line gradually decreases and becomes negligible (Figure S21). While Ir anions accumulate and reach high concentrations, the rapid (re-)absorption of cationic Ir back into the ionomer phase results in a low steady-state concentration of the cations in the recirculation loop. Consequently, the fraction of cationic Ir diminishes over time. Similar trends are observed for other ions as measured by ion chromatography (IC). While the concentrations of anionic species (F^-, Cl^-, N^{3-}, NO_3^-, SO_4^{2-}) continue to increase over time (Table S1), the concentration of cationic species (Ca^{2+}, Na^+, K^+, Mg^+) remains roughly constant over longer periods of operation with recirculation flow (Table S2).

3.3.2. Sinks for Ir anions under anode water recirculation

As discussed before, Ir in the recirculated anode water line becomes predominantly anionic with increased operating time as these species can accumulate to higher concentrations. However, there may be more sluggish sink terms that become significant at elevated concentrations. A combined experimental and model-based approach is used to analyze the transport and sinks of the anionic Ir species. The cell was operated at a constant current density of 0.8 A/cm^2 for ca. 100 h with water

recirculation at the anode side. The total water volume was either kept constant by replenishing water to compensate for water loss due to consumption and electroosmotic drag, or allowed to decrease by stopping replenishment. A small anode bubbler volume was used (volume profile in Fig. 8) in order to facilitate the Ir accumulation process. The ACL can be considered to be in a stabilized state due to the previous extended testing in single-pass flow mode for more than 75 h (Fig. 4).

As a result of the OER-induced dissolution process, the Ir concentration shows a continuous increase until ca. 49 h. At this time, water replenishment was temporarily stopped for the second time. As the liquid volume decreases, the Ir species are concentrated, resulting in a sharp increase in Ir concentration at ca. 50 h (Fig. 8a). When water replenishment is resumed at ca. 52 h, the water volume becomes constant again. At this point, the concentration of Ir is very high, resulting in a rate of back-transport into the CCM that exceeds the rate of the ongoing OER-related Ir dissolution process (Fig. 8b). Consequently, the concentration of Ir decreases. Figure S22 illustrates the anticipated concentration profile in the hypothetical absence of a sink.

This decrease provides clear evidence that there is also a significant sink for anionic Ir species within the water loop, even when using a test station designed to minimize galvanic displacement. The model, parameterized through separate Ir deposition tests of Ir on different metal surfaces (SI Section 7), confirms that the deposition rates on the flow field and PTL surfaces are negligible (Fig. 8b). Since the relative fraction of Ir cations in the recirculated water loop is negligible (Figure S21 and discussion Section 3.3.1), a steady-state Ir concentration in the recirculation loop is established (t > 100 h, Fig. 8) when the dissolution rate of Ir anions becomes equal to the rate at which they are transported back into the CCM:

$$c_{m-,SS} = \frac{j \; x_{m-}}{S_{N,w} \; z_{O_2} \; F \; k_{bt,m-}} \qquad (2)$$

3.3.3. What happens to Ir anions transported back into the CCM?

With $k_{bt,m-}$ defined as a generic model parameter (eqn. S17), the discussion has yet to address whether the anionic Ir transported back into the CCM is deposited in the ACL or remains in ionic form and transported further toward the cathode side. Insight can be gained by examining the two periods after switching back from recirculation to single-pass flow mode (SP1 and SP2, Fig. 8). It is observed that the Ir dissolution flux after switching back is much higher than the flux measured prior to the recirculation period. Figure S24 shows that it takes a long time, about 18 hours of operation, for the Ir dissolution flux to return to the pre-recirculation level. Surprisingly, the 'excess amount' of Ir, which is released during the subsequent single-pass flow mode until the moment the dissolution rate returns to the pre-recirculation level, corresponds to the total amount of Ir species removed from the anode water loop during the preceding 101 h of operation with water recirculation (Fig. 9), suggesting that the higher dissolution rate after
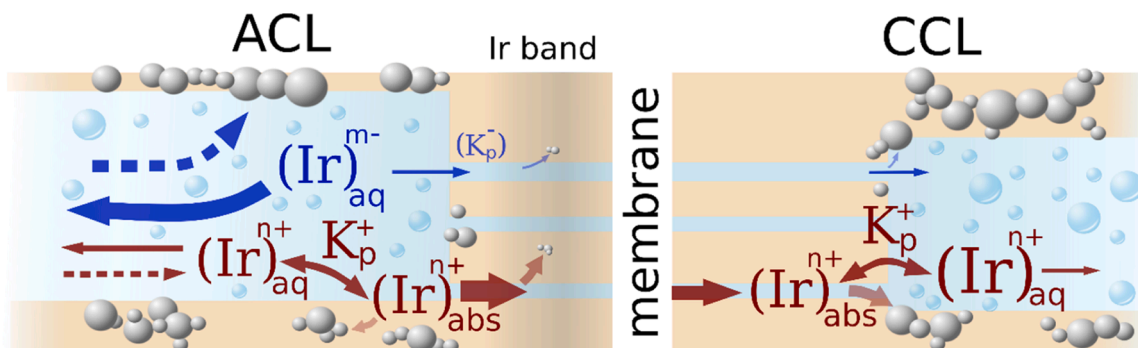

Fig. 7. Proposed mechanism of transport, absorption and desorption of Ir species. Dissolution and deposition processes take place in different locations (e.g. ACL, Ir band, CCL). Transport processes displayed by dashed arrows occur under water recirculation mode. K_p is the partition coefficient describing the equilibrium of absorption and desorption of the Ir species. Blue and beige colors represent aqueous channels and ionomer phase, respectively.
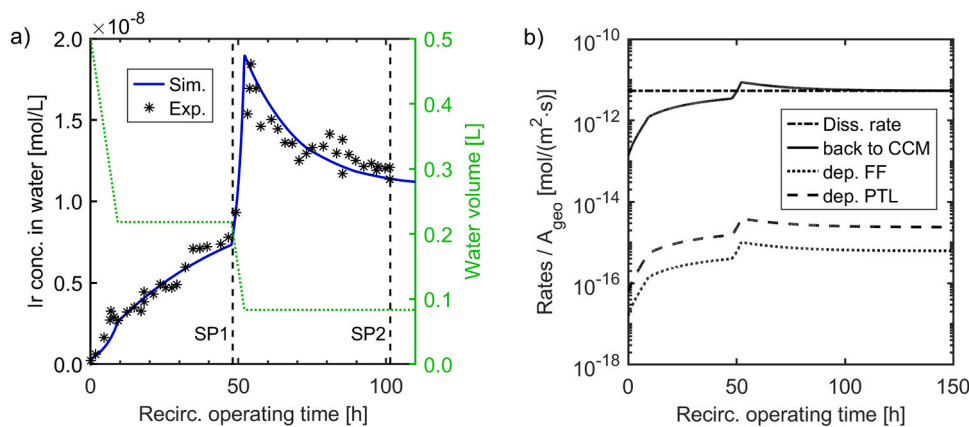
Fig. 8. a) Measured Ir concentration in the anode water bubbler (black stars) and model simulation (blue line). 'SP1' and 'SP2' indicate the two periods of single-pass water flow operation (Fig. S23). The experimental time of the x-axis excludes OCP phases (displayed in Fig. S23 as dashed lines) and single-pass water flow periods. The water volume in the anode bubbler is displayed in green. b) Simulated transport and reaction rates of Ir anions normalized by the geometric surface area. The lines represent the dissolution rate (dash-dot), the rate of transport (and/or deposition) back into the CCM (solid), the deposition rate on the surface of the flow field (dotted) and on the Pt-coated PTL (dashed).
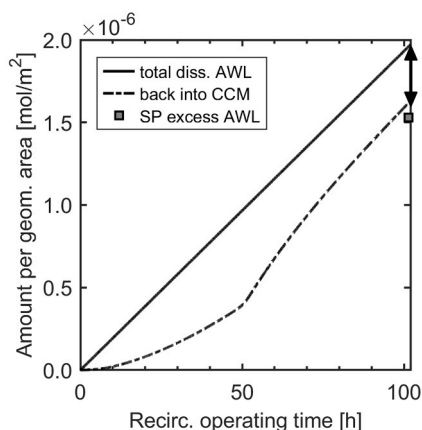
Fig. 9. Simulated and measured amount of Ir over time. The solid line represents the total amount of anionic Ir transported into the anode water line (AWL) as a result of the OER induced Ir dissolution process. The dashed-dotted line represents the total amount of the anionic Ir species transported from the water recirculation loop back into the CCM. The square symbol displays the 'excess' Ir amount that was released into the water phase during the two single-pass water flow interims (SP1 and SP2 in Fig. 7a) until the moment the dissolution rate decreased back to the pre-recirculation level. For the 'excess amount' (grey shading in Fig. S24), the quantity of Ir anticipated based on the pre-recirculation Ir dissolution flux is already subtracted. The arrow represents the experimentally measured Ir amount in the AWL at the end of the recirculation test.

switching back to the single-pass flow mode is caused by the release of Ir ions previously stored during water recirculation. Further support for this explanation is provided by analyzing the anionic and cationic Ir fractions via absorption experiments. The pre-recirculation dissolution rate includes a cationic fraction of 0.24 (Figure S19), whereas a very low cationic fraction of ca. 0.05 (Figure S21) was measured after 0.6 h of switching to SP2 (Figure S24). If the excess Ir flux measured at this time (Figure S24, red arrow) is due to the release of previously stored anionic Ir species, a cationic fraction of 0.04 is calculated, which is in close agreement with the measured fraction. Despite their accumulation in the recirculated water loop, Ir anions are not significantly transported to the cathode side for the reasons discussed in Section 3.3.1.

It is noteworthy that the calculation of the amount of Ir that 'disappeared' from the anode water line during the recirculation period does not require a complex model, but follows a simple mass balance (101 h, Fig. 9), which considers the stability-number measured prior to the recirculation period (section 1.4). An approximately constant stability-number can be expected, as the catalyst is in a stabilized state due to the previous operation in single-pass flow mode. Only two parameters were estimated by fitting the dynamic data, the rate constant $k_{bt,m-}$ and $S_{N,w}$. The value of $S_{N,w} = 2.62 \bullet 10^9$ is very close to the value of ca. $2.5 \bullet 10^9$ measured in single-pass flow under similar operating conditions prior to the water recirculation experiment, which is an indication of the validity of the chosen model assumptions.

Three domains could be responsible for the observed storage and release effect of the anionic Ir species; (i) the water phase, (ii) the membrane phase, and (iii) the ACL region. The storage in the water phase (i) seems unrealistic, as the release is expected to occur quickly due to both diffusion and bubble-induced mixing, rather than over a period of 18 hours. The large amount stored during recirculation, which is ca. 3.6 times the amount of Ir in the anode water loop at the end of the recirculation test (Fig. 8), contrasts with the low storage capacity of the membrane domain (ii), indicated by the negligible uptake of Ir from the recirculation loop in the absorption test conducted using a fresh CEM (Figure S21). Noteworthy, overnight off phases with N_2 purging in the cathode side during the recirculation test (Figure S23) did not induce any significant release of stored amounts into the water recirculation loop. Ir anions transported to the cathode side do not accumulate because they are easily transported further to the cathode water line due to their low absorption affinity and the bubbling conditions, if not first deposited on the Pt particles.

Therefore, in reference to (iii), it is suggested that the anionic Ir species are stored via (re-)deposition on the catalyst particles in the ACL. The observations indicate that the deposited Ir species are stabilized at high Ir concentrations in the recirculated water flow. However, when the concentration of water-dissolved Ir species is drastically reduced by switching back to single-pass water flow, the Ir deposits are slowly dissolved under oxygen evolving conditions and washed out through the cell outlet. The stabilization of the deposits at higher Ir concentrations may be the result of a shift in the Nernst-potential [6,38]. This influence is of mechanistic interest because Ir cations that remain preferentially absorbed in the ionomer or membrane phases, possibly 'trapped' between the interface of the ACL with the water phase on the one side and the Ir band on the other side, may have a similar stabilizing effect on the catalyst surface, contributing to the significantly higher stability in the MEA-setup in comparison to the half-cell environment. It has been proposed that a stabilizing concentration effect and redeposition of dissolved products can have a positive impact on ACL longevity [6,38, 51], which may provide technical avenues to improve electrocatalytic

stability.

It is noted that water recirculation leads to an increased concentration of impurities, as indicated by the IC measurements (Table S1 and Table S2) and the higher water conductivity of 18 μS/cm, due to the long operation with a very low bubbler volume of 80 mL, although the water consumption was compensated by purified water with a controlled conductivity of 0.055 μS/cm during the constant volume interims of the recirculation test. Impurities could result in an increased dissolution rate, as for example has been observed for Au [52]. Nevertheless, it appears unlikely that a 3.5-fold increase in the dissolution rate (or even higher) occurred during the recirculation compared to the pre-recirculation level (Figure S24) as a result of the low impurity concentrations, considering that the cathode water line measurements do not indicate an elevated dissolution rate at the end of the recirculation period (Figure S23b) compared to that at the beginning. Measurements in test station B also showed a significantly increased Ir dissolution flux that persisted for several hours after switching from recirculation back to single-pass flow (Figure S26), despite a lower conductivity of the recirculated water of only 1 μS/cm. This further supports the view that the transient high dissolution rate upon switching back to single-pass is mainly due to the release of previously stored Ir anions. Furthermore, the assumption of an impurity-related decrease in the stability-number (Figure S27) to explain the increased Ir dissolution flux during SP1 and SP2 did not result in a good fit of the mathematical model with the experimental data (Figure S28).

3.4. Importance of single-pass water flow for stability testing

The clear experimental evidence of a significant sink for both Ir cations and anions from the anode water line into the CCM (Section 3.3.2) implies that at longer times, the assessment of catalyst stability and ACL lifetime based on dissolution measurements with water recirculation leads to inaccurate estimations, including physically irrational outcomes such as $S_{N,w} \to \infty$ or $S_{N,w} < 0$ (Fig. 8). Therefore, it is suggested that single-pass flow mode is preferable for PEMWE catalyst dissolution testing in order to effectively minimize the occurrence of back-transport of water-dissolved dissolution products. Noteworthy, the single-pass flow of pure water into the cell mimics the common technical implementation of PEMWEs, where the water recirculation loop is continuously purified using ion exchange resins [53]. Additional tests demonstrate that the measured Ir dissolution flux is independent of the applied flow rate, further supporting the validity of the single-pass approach (Figure S29).

It has been suggested that when the catalyst is in a stabilized state, the overall dissolution rate can be approximated based on the Ir dissolution flux measured in single-pass flow mode, since dissolved anionic Ir species are primarily transported into the anode water line and the lattice rupture that occurs under OER conditions generates Ir anions and cations in a roughly constant ratio [14]. Under these assumptions, it has been deduced that the total Ir dissolution rate can be estimated by multiplying the Ir dissolution flux measured in single-pass flow by a factor of 3.7 [14]. Therefore, the measurement of Ir in the anode water line in single-pass flow mode provides a practical approach to approximate Ir dissolution in the zero-gap PEMWE setup, which is not limited to short operating times. For the smaller cell used in this study (8.4 cm²), only 302 mL/h of purified water was required to maintain the operation in single-pass flow mode (3 A/cm² at an iR-free potential of 1.55 V). For future studies with larger cells or even stacks, a possible approach could involve continuously purifying the recirculated anode water line using ion exchange materials, while sampling at the cell outlet to simulate single-pass water flow test conditions.

3.5. ACL lifetime estimation

A quasi-steady-state lifetime estimation is conducted for the PEMWE ACL. The ACL lifetime is predicted (Fig. 10, solid lines) based on the
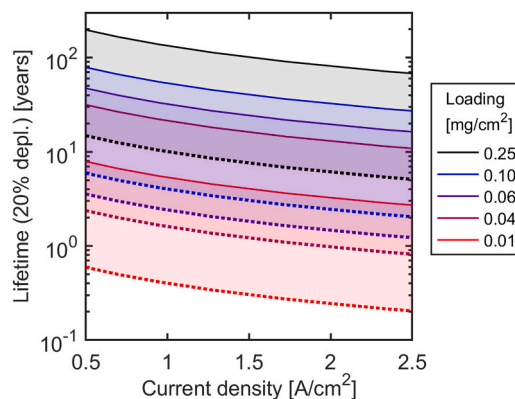
Fig. 10. Lifetime estimation of IrOx catalyst in PEMWE for different catalyst loadings for steady-state operation depending on the applied current density. Solid lines are calculated based on the stability-number measured after 630 h of operation in single-pass water flow mode. In order to obtain upper and lower bounds, a second estimation was added: The dotted lines represent the lifetime estimation based on measurements from [21]. The stability-number data is projected to 630 h using the reciprocal dependence on time (Eq. 1), as visualized by the green solid line in Fig. 4. A factor of 3.7 is used in both estimations (dotted and solid lines) to account for dissolved Ir species transported in the cathode direction [14]. Further details on the calculations are provided in SI Section 8.

stability-number measured after 630 h of operation (Fig. 4, red circles). The aforementioned factor of 3.7 is used as an approximation to account for the amount of Ir transported in the cathode direction. The current density dependence is calculated from the stability-number values shown in Fig. 6a. Despite the initially higher rates of Ir dissolution, the amount of Ir that is lost during 630 h of steady-state operation (Fig. 4, red circles) is estimated to be small (ca. 520 ng/cm²) and can be considered negligible for lifetime estimations in the order of 10 years. A detailed description of the calculation is provided in SI Section 8.

The results show that accounting for extended experimental times, e. g. 630 h, has a significant impact on lifetime predictions. It is estimated that commercially available catalyst materials, such as those used in this study, could already enable stable, steady-state operation for ten years (87600 h) at Ir loadings as low as ca. 0.04 mg/cm² (Fig. 10), provided that there is an ideal catalyst layer or cell design that preserves both the protonic and electrical connectivity [26,28] within the catalyst layer. Despite high fractions of Ir material remaining in the ACL, catalyst dissolution may disrupt particle percolation [34]. In this context, studies have shown that alternative approaches, such as sputtering the Ir catalyst onto the PTL [24,54] or incorporating catalyst support materials [28], promote effective percolation, enabling high catalyst utilization and a good performance even at very low Ir loadings. Therefore, such approaches may be advantageous also for maintaining catalyst percolation over the targeted lifetimes.

The conducted lifetime analysis has several limitations: (1) The catalyst stability after steady-state operation for 630 h was considered in this estimation. In practice, the catalyst may further stabilize over longer operation periods or possibly destabilize due to intermittent operation. Therefore, it is suggested that future studies should investigate Ir dissolution and its time stabilization behavior in the MEA setup under intermittent operating profiles [55], which can be performed using the single-pass flow mode proposed herein. (2) The factor 3.7 does not account for possible redeposition of dissolved Ir cations on the catalyst particles, which may reduce the loss of catalyst material. (3) For simplicity, ACL lifetime is defined as the duration over which 20 % of the Ir material is dissolved. In practice, ACLs designed with higher Ir loadings may allow for a greater relative loss of Ir material while still maintaining effective percolation among the catalyst particles. Despite the limitations, the analysis provides first insights into ACL longevity

depending on current density and catalyst loading based on measurements in the realistic zero-gap PEMWE configuration. The difference between the solid and the dotted lines in Fig. 10, despite the use of the same IrOx catalyst, could stem from factors such as the CCM design (commercial CCMs herein vs. in-house CCM fabrication using decal transfer [21]) or the clamping force of the cell. The observed difference emphasizes that optimization of the catalyst material is not the only way to enhance the electrocatalytic stability, but there is a substantial potential for improvement by systematically evaluating the influences of cell design and ACL properties and architecture, which can be studied using the single-pass flow mode.

4. Conclusions

In this work, Ir catalyst dissolution in the PEMWE MEA-setup was measured in the anode and cathode water lines to study the influence of time and current density on Ir dissolution and to analyze the transport and deposition behavior of Ir species dissolved in the water domain. The cell anode was fed in either single-pass or water recirculation mode. It is demonstrated that the former approach allows for a quasi-online measurement of catalyst dissolution in a realistic MEA-setup, closely relevant to industrial applications. The initially high dissolution rate of Ir decreases significantly during operation, following a reciprocal relationship with time. This behavior can be mechanistically explained by a kinetic stabilization reaction that exhibits a quadratic reaction order with regard to the density of unstable sites. As the system stabilizes, a quasi-steady-state relationship between dissolution and current density emerges due to the mechanistic coupling of Ir dissolution and OER. The stability-number is highly sensitive to the polarization, increasing by more than two orders of magnitude with current density. A linear relationship between Ir dissolution and current density is established above ca. 1.6 A/cm^2.

The transport of dissolved Ir species depends not only on their charge but also on the anode water feed mode, single-pass or recirculation. In water recirculation mode, cationic Ir dissolution products are effectively reabsorbed by the ionomer or membrane phase, while higher accumulation can be observed for anionic Ir species due to their low absorption affinity. However, clear evidence of back-transport into the CCM was also found for these species. Model-based analysis suggests that Ir species redeposit in the ACL and are stabilized by high concentrations of Ir ions, but de-stabilized when pure water is introduced into the cell in single-pass flow mode. The application of single-pass water flow is recommended for catalyst stability testing as it adds valuable time-resolved insights to electrochemical degradation testing and post-test CCM analysis. Measurements in this flow mode can be used to approximate the total dissolution of Ir in the zero-gap configuration, allowing assessment of Ir dissolution over extended test periods. Lifetime analysis indicates that, due to the strong stabilization with time, commercial Ir oxide materials may already be capable of sustaining 10 years of steady-state operation with Ir loadings as low as 0.04 mg/cm^2, provided there is an optimal catalyst layer design that maintains both the protonic and electrical connectivity of the nanoparticles. Future studies can explore the impact of intermittent operation on Ir dissolution in the MEA-setup, utilizing the proposed single-pass water flow mode.

CRediT authorship contribution statement

An Phuc Dam: Conceptualization, Methodology, Investigation, Writing - Original Draft, Software, Visualization. Tobias Franz: Conceptualization, Investigation, Writing -Review & Editing. Georgios Papakonstantinou: Conceptualization, Methodology, Writing - Review & Editing, Supervision. Kai Sundmacher: Conceptualization, Writing -Review & Editing, Supervision, Funding acquisition.

Declaration of Generative AI and AI-assisted technologies in the writing process

During the preparation of this work the authors used DeepL and ChatGPT in order to improve language and readability. After using this tool/service, the authors reviewed and edited the content as needed and take full responsibility for the content of the publication.

Declaration of Competing Interest

The authors declare that they have no known competing financial interests or personal relationships that could have appeared to influence the work reported in this paper.

Acknowledgements

Appendix A. Supporting information

Supplementary data associated with this article can be found in the online version at doi:10.1016/j.apcatb.2024.124946.

Data availability

Data will be made available on request.

References

[1] S. Kiemel, T. Smolinka, F. Lehner, J. Full, A. Sauer, R. Miehe, Critical materials for water electrolysers at the example of the energy transition in Germany, Int. J. Energy Res. 45 (2021) 9914–9935, https://doi.org/10.1002/er.6487.

[2] U. Babic, M. Suermann, F.N. Büchi, L. Gubler, T.J. Schmidt, Critical review—identifying critical gaps for polymer electrolyte water electrolysis development, J. Electrochem. Soc. 164 (2017) F387–F399, https://doi.org/10.1149/2.1441704jes.

[3] M.A. Hubert, L.A. King, T.F. Jaramillo, Evaluating the case for reduced precious metal catalysts in proton exchange membrane electrolyzers, ACS Energy Lett. 7 (2022) 17–23, https://doi.org/10.1021/acsenergylett.1c01869.

[4] C. Minke, M. Suermann, B. Bensmann, R. Hanke-Rauschenbach, Is iridium demand a potential bottleneck in the realization of large-scale PEM water electrolysis? Int. J. Hydrog. Energy 46 (2021) 23581–23590, https://doi.org/10.1016/j.ijhydene.2021.04.174.

[5] S.M. Alia, S. Stariha, R.L. Borup, Electrolyzer durability at low catalyst loading and with dynamic operation, J. Electrochem. Soc. 166 (2019) F1164–F1172, https://doi.org/10.1149/2.0231915jes.

[6] S. Geiger, O. Kasian, M. Ledendecker, E. Pizzutilo, A.M. Mingers, W.T. Fu, O. Diaz-Morales, Z. Li, T. Oellers, L. Fruchter, A. Ludwig, K.J.J. Mayrhofer, M.T.M. Koper, S. Cherevko, The stability number as a metric for electrocatalyst stability benchmarking, Nat. Catal. 1 (2018) 508–515, https://doi.org/10.1038/s41929-018-0085-6.

[7] O. Kasian, J.-P. Grote, S. Geiger, S. Cherevko, K.J.J. Mayrhofer, The common intermediates of oxygen evolution and dissolution reactions during water electrolysis on iridium, Angew. Chem. 57 (2018) 2488–2491, https://doi.org/10.1002/anie.201709652.

[8] O. Kasian, S. Geiger, T. Li, J.-P. Grote, K. Schweinar, S. Zhang, C. Scheu, D. Raabe, S. Cherevko, B. Gault, K.J.J. Mayrhofer, Degradation of iridium oxides via oxygen evolution from the lattice: correlating atomic scale structure with reaction mechanisms, Energy Environ. Sci. 12 (2019) 3548–3555.

[9] Y.-T. Kim, P.P. Lopes, S.-A. Park, A.-Y. Lee, J. Lim, H. Lee, S. Back, Y. Jung, N. Danilovic, V. Stamenkovic, J. Erlebacher, J. Snyder, N.M. Markovic, Balancing activity, stability and conductivity of nanoporous core-shell iridium/iridium oxide oxygen evolution catalysts, Nat. Commun. 8 (2017) 1449, https://doi.org/10.1038/s41467-017-01734-7.

[10] Z. Yu, Y. Li, A. Torres-Pinto, A.P. LaGrow, V.M. Diaconescu, L. Simonelli, M. J. Sampaio, O. Bondarchuk, I. Amorim, A. Araujo, A.M. Silva, C.G. Silva, J.L. Faria, L. Liu, Single-atom Ir and Ru anchored on graphitic carbon nitride for efficient and

stable electrocatalytic/photocatalytic hydrogen evolution, Appl. Catal. B: Environ. 310 (2022) 121318, https://doi.org/10.1016/j.apcatb.2022.121318.

[11] M. You, Y. Xu, B. He, J. Zhang, L. Gui, J. Xu, W. Zhou, L. Zhao, Realizing robust and efficient acidic oxygen evolution by electronic modulation of 0D/2D CeO2 quantum dots decorated SrIrO3 nanosheets, Appl. Catal. B: Environ. 315 (2022) 121579, https://doi.org/10.1016/j.apcatb.2022.121579.

[12] A.P. Dam, G. Papakonstantinou, K. Sundmacher, On the role of microkinetic network structure in the interplay between oxygen evolution reaction and catalyst dissolution, Sci. Rep. 10 (2020) 14140, https://doi.org/10.1038/s41598-020-69723-3.

[13] T. Binninger, R. Mohamed, K. Waltar, E. Fabbri, P. Levecque, R. Kötz, T.J. Schmidt, Thermodynamic explanation of the universal correlation between oxygen evolution activity and corrosion of oxide catalysts, Sci. Rep. 5 (2015) 12167.

[14] A.P. Dam, B.Y.A. Abuthaher, G. Papakonstantinou, K. Sundmacher, Insights into the path-dependent charge of iridium dissolution products and stability of electrocatalytic water splitting, J. Electrochem. Soc. 170 (2023) 64504, https://doi.org/10.1149/1945-7111/acd4f2.

[15] D.A. Fine, Studies of the iridium(III) and (IV)—chloride system in acid solution, J. Inorg. Nucl. Chem. 32 (1970) 2731–2742, https://doi.org/10.1016/0022-1902(70)80323-2.

[16] R. Zhang, N. Dubouis, M. Ben Osman, W. Yin, M.T. Sougrati, D.A.D. Corte, D. Giaume, A. Grimaud, A dissolution/precipitation equilibrium on the surface of iridium-based perovskites controls their activity as oxygen evolution reaction catalysts in acidic media, Angew. Chem. 58 (2019) 4571–4575.

[17] R. Kötz, H. Neff, S. Stucki, Anodic iridium oxide films: xps-studies of oxidation state changes and, J. Electrochem. Soc. 131 (1984) 72–77, https://doi.org/10.1149/1.2115548.

[18] M. Pourbaix. Atlas of electrochemical equilibria in aqueous solutions, 2nd ed., National Association of Corrosion Engineers, Houston, Tex., 1974.

[19] A. Lončar, D. Escalera-López, S. Cherevko, N. Hodnik, Inter-relationships between oxygen evolution and iridium dissolution mechanisms, Angew. Chem. (Int. Ed. Engl.) (2021) e202114437, https://doi.org/10.1002/anie.202114437.

[20] G. Papakonstantinou, I. Spanos, A.P. Dam, R. Schlögl, K. Sundmacher, Electrochemical evaluation of the de-/re-activation of oxygen evolving Ir oxide, Phys. Chem. Chem. Phys. 24 (2022) 14579–14591, https://doi.org/10.1039/d2cp00828a.

[21] J. Knöppel, M. Möckl, D. Escalera-López, K. Stojanovski, M. Bierling, T. Böhm, S. Thiele, M. Rzepka, S. Cherevko, On the limitations in assessing stability of oxygen evolution catalysts using aqueous model electrochemical cells, Nat. Commun. 12 (2021) 2231, https://doi.org/10.1038/s41467-021-22296-9.

[22] K. Ehelebe, D. Escalera-López, S. Cherevko, Limitations of aqueous model systems in the stability assessment of electrocatalysts for oxygen reactions in fuel cell and electrolyzers, Curr. Opin. Electrochem. 29 (2021) 100832, https://doi.org/10.1016/j.coelec.2021.100832.

[23] H. Yu, L. Bonville, J. Jankovic, R. Maric, Microscopic insights on the degradation of a PEM water electrolyzer with ultra-low catalyst loading, Appl. Catal. B: Environ. 260 (2020) 118194, https://doi.org/10.1016/j.apcatb.2019.118194.

[24] A. Li, S. Kong, K. Adachi, H. Ooka, K. Fushimi, Q. Jiang, H. Ofuchi, S. Hamamoto, M. Oura, K. Higashi, T. Kaneko, T. Uruga, N. Kawamura, D. Hashizume, R. Nakamura, Atomically dispersed hexavalent iridium oxide from MnO2 reduction for oxygen evolution catalysis, Sci. (N. Y., N. Y.) 384 (2024) 666–670, https://doi.org/10.1126/science.adg5193.

[25] G. Papakonstantinou, G. Algara-Siller, D. Teschner, T. Vidaković-Koch, R. Schlögl, K. Sundmacher, Degradation study of a proton exchange membrane water electrolyzer under dynamic operation conditions, Appl. Energy 280 (2020) 115911, https://doi.org/10.1016/j.apenergy.2020.115911.

[26] S. Higashi, A. Beniya, Ultralight conductive IrO2 nanostructured textile enables highly efficient hydrogen and oxygen evolution reaction: importance of catalyst layer sheet resistance, Appl. Catal. B: Environ. 321 (2023) 122030, https://doi.org/10.1016/j.apcatb.2022.122030.

[27] Z. Xie, L. Ding, S. Yu, W. Wang, C.B. Capuano, A. Keane, K. Ayers, D.A. Cullen, H. M. Meyer, F.-Y. Zhang, Ionomer-free nanoporous iridium nanosheet electrodes with boosted performance and catalyst utilization for high-efficiency water electrolyzers, Appl. Catal. B: Environ. 341 (2024) 123298, https://doi.org/10.1016/j.apcatb.2023.123298.

[28] H. Kim, J. Kim, J. Kim, G.H. Han, W. Guo, S. Hong, H.S. Park, H.W. Jang, S.Y. Kim, S.H. Ahn, Dendritic gold-supported iridium/iridium oxide ultra-low loading electrodes for high-performance proton exchange membrane water electrolyzer, Appl. Catal. B: Environ. 283 (2021) 119596, https://doi.org/10.1016/j.apcatb.2020.119596.

[29] H.B. Tao, H. Liu, K. Lao, Y. Pan, Y. Tao, L. Wen, N. Zheng, The gap between academic research on proton exchange membrane water electrolysers and industrial demands, Nature nanotechnology. https://doi.org/10.1038/s41565-024-01699-x.

[30] M.J. Burch, K.A. Lewinski, M.I. Buckett, S. Luopa, F. Sun, E.J. Olson, A. J. Steinbach, A novel work-flow to study Ir electrode thinning and dissolution in proton exchange membrane water electrolyzers, J. Power Sources 500 (2021) 229978, https://doi.org/10.1016/j.jpowsour.2021.229978.

[31] M. Milosevic, T. Böhm, A. Körner, M. Bierling, L. Winkelmann, K. Ehelebe, A. Hutzler, M. Suermann, S. Thiele, S. Cherevko, In search of lost iridium: quantification of anode catalyst layer dissolution in proton exchange membrane water electrolyzers, ACS Energy Lett. (2023) 2682–2688, https://doi.org/10.1021/acsenergylett.3c00193.

[32] M. Stähler, A. Burdzik, I. Friedrich, A. Everwand, F. Scheepers, Oxygen flow rate measurement as a whistleblower for degradation effects in PEM water electrolysis,

Int. J. Hydrog. Energy 78 (2024) 682–687, https://doi.org/10.1016/j.ijhydene.2024.06.334.

[33] U. Babic, M. Tarik, T.J. Schmidt, L. Gubler, Understanding the effects of material properties and operating conditions on component aging in polymer electrolyte water electrolyzers, J. Power Sources 451 (2020) 227778, https://doi.org/10.1016/j.jpowsour.2020.227778.

[34] S.M. Alia, K.S. Reeves, H. Yu, J. Park, N. Kariuki, A.J. Kropf, D.J. Myers, D. A. Cullen, Electrolyzer performance loss from accelerated stress tests and corresponding changes to catalyst layers and interfaces, J. Electrochem. Soc. 169 (2022) 54517, https://doi.org/10.1149/1945-7111/ac697e.

[35] A. Weiß, A. Siebel, M. Bernt, T.-H. Shen, V. Tileli, H.A. Gasteiger, Impact of intermittent operation on lifetime and performance of a PEM water electrolyzer, J. Electrochem. Soc. 166 (2019) F487–F497, https://doi.org/10.1149/2.0421908jes.

[36] P. Lettenmeier, R. Wang, R. Abouatallah, S. Helmly, T. Morawietz, R. Hiesgen, S. Kolb, F. Burggraf, J. Kallo, A.S. Gago, K.A. Friedrich, Durable membrane electrode assemblies for proton exchange membrane electrolyzer systems operating at high current densities, Electrochim. Acta 210 (2016) 502–511, https://doi.org/10.1016/j.electacta.2016.04.164.

[37] C. Wei, Z. Wang, K. Otani, D. Hochfilzer, K. Zhang, R. Nielsen, I. Chorkendorff, J. Kibsgaard, Benchmarking electrocatalyst stability for acidic oxygen evolution reaction: the crucial role of dissolved ion concentration, ACS Catal. (2023) 14058–14069, https://doi.org/10.1021/acscatal.3c03257.

[38] J. Zhu, L. Li, M. Cao, Le Chatelier's principle to stabilize intrinsic surface structure of oxygen-evolving catalyst for enabling ultra-high catalytic stability of zinc-air battery and water splitting, Nano Energy 122 (2024) 109300, https://doi.org/10.1016/j.nanoen.2024.109300.

[39] A.M. Moschovi, E. Zagoraiou, E. Polyzou, I. Yakoumis, Recycling of critical raw materials from hydrogen chemical storage stacks (PEMWE), membrane electrode assemblies (MEA) and electrocatalysts, IOP Conf. Ser.: Mater. Sci. Eng. 1024 (2021) 12008, https://doi.org/10.1088/1757-899X/1024/1/012008.

[40] M. Carmo, G.P. Keeley, D. Holtz, T. Grube, M. Robinius, M. Müller, D. Stolten, PEM water electrolysis: innovative approaches towards catalyst separation, recovery and recycling, Int. J. Hydrog. Energy 44 (2019) 3450–3455, https://doi.org/10.1016/j.ijhydene.2018.12.030.

[41] S. Czioska, A. Boubnov, D. Escalera-López, J. Geppert, A. Zagalskaya, P. Röse, E. Saraçi, V. Alexandrov, U. Krewer, S. Cherevko, J.-D. Grunwaldt, Increased Ir–Ir interaction in iridium oxide during the oxygen evolution reaction at high potentials probed by operando spectroscopy, ACS Catal. 11 (2021) 10043–10057, https://doi.org/10.1021/acscatal.1c02074.

[42] S. Cherevko, S. Geiger, O. Kasian, A. Mingers, K.J. Mayrhofer, Oxygen evolution activity and stability of iridium in acidic media. Part 2. – electrochemically grown hydrous iridium oxide, J. Electroanal. Chem. 774 (2016) 102–110, https://doi.org/10.1016/j.jelechem.2016.05.015.

[43] S.M. Alia, B. Rasimick, C. Ngo, K.C. Neyerlin, S.S. Kocha, S. Pylypenko, H. Xu, B. S. Pivovar, Activity and durability of iridium nanoparticles in the oxygen evolution reaction, F3105-F3112, J. Electrochem. Soc. 163 (2016), https://doi.org/10.1149/2.0151611jes.

[44] P.T. Landsberg, On the logarithmic rate law in chemisorption and oxidation, J. Chem. Phys. 23 (1955) 1079–1087, https://doi.org/10.1063/1.1742193.

[45] M. Zlobinski, U. Babic, M. Fikry, L. Gubler, T.J. Schmidt, P. Boillat, Dynamic neutron imaging and modeling of cationic impurities in polymer electrolyte water electrolyzer, J. Electrochem. Soc. 167 (2020) 144509, https://doi.org/10.1149/1945-7111/abc83b.

[46] H. Miyoshi, M. Chubachi, M. Yamagami, T. Kataoka, Characteristic coefficients for equilibrium between solution and Neosepta or Selemion cation exchange membranes, J. Chem. Eng. Data 37 (1992) 120–124, https://doi.org/10.1021/je00005a031.

[47] M. Ersöz, S. Yildiz, The sorption of metals on the polysulfone cation exchange membranes, Turk. J. Chem. 25 (2001) 39–48.

[48] A.G. Guzmán-Garcia, P.N. Pintauro, M.W. Verbrugge, R.F. Hill, Development of a space-charge transport model for ion-exchange membranes, AIChE J. 36 (1990) 1061–1074, https://doi.org/10.1002/aic.690360713.

[49] D.M. Ruthven, Principles of adsorption and adsorption processes, Wiley, New York, 1984.

[50] S. Ben-Shebil, A. Alkan-Sungur, A.R. Özdural, Fixed-bed ion exchange columns operating under non-equilibrium conditions: estimation of mass transfer properties via non-equilibrium modeling, React. Funct. Polym. 67 (2007) 1540–1547, https://doi.org/10.1016/j.reactfunctpolym.2007.07.040.

[51] A.E. Thorarinsdottir, S.S. Veroneau, D.G. Nocera, Self-healing oxygen evolution catalysts, Nat. Commun. 13 (2022) 1243, https://doi.org/10.1038/s41467-022-28723-9.

[52] O. Kasian, N. Kulyk, A. Mingers, A.R. Zeradjanin, K.J. Mayrhofer, S. Cherevko, Electrochemical dissolution of gold in presence of chloride and bromide traces studied by on-line electrochemical inductively coupled plasma mass spectrometry, Electrochim. Acta 222 (2016) 1056–1063, https://doi.org/10.1016/j.electacta.2016.11.074.

[53] I.S.E. Fraunhofer, 2021, Fraunhofer I.S.E., Cost Forecast for Low-Temperature Electrolysis - Technology Driven Bottom-Up Prognosis for PEM and Alkaline Water Electrolysis Systems, 2021.

[54] J.K. Lee, G. Anderson, A.W. Tricker, F. Babbe, A. Madan, D.A. Cullen, J.D. Arregui-Mena, N. Danilovic, R. Mukundan, A.Z. Weber, X. Peng, Ionomer-free and recyclable porous-transport electrode for high-performing proton-exchange-membrane water electrolysis, Nat. Commun. 14 (2023) 4592, https://doi.org/10.1038/s41467-023-40375-x.

[55] A. Buttler, H. Spliethoff, Current status of water electrolysis for energy storage, grid balancing and sector coupling via power-to-gas and power-to-liquids, Renew. Sustain. Energy Rev. 82 (2018) 2440–2454, https://doi.org/10.1016/j.rser.2017.09.003.